Dynamics of the Jet Flow Issued from a Lobed Nozzle: Tomographic Particle Image Velocimetry Measurements

Chuangxin HE[1, 2], Yingzheng LIU[1]* & Lian GAN[3]

[1] *Key Lab of Education Ministry for Power Machinery and Engineering*
School of Mechanical Engineering, Shanghai Jiao Tong University
Shanghai 200240, China

[2] *Key Laboratory of Aerodynamic Noise Control, China Aerodynamics Research and Development Center, Mianyang, Sichuan 621000, China*

[3] *Department of Engineering, Durham University*
Durham DH1 3LE, UK

Manuscript revised in February 2021

* Corresponding author:
*E-mail address:*yzliu@sjtu.edu.cn

Abstract

This study focuses on the dynamics of the three-dimensional jet flow issued from a lobed nozzle. Flow field measurements were performed using a split-screen dual-camera tomographic particle image velocimetry (tomo-PIV) system. The lobed nozzle was constructed using three-circle configuration at the nozzle exit, where the ratio of the circular centre offset to the circle radius was $a/b = 0.8$. Two high-speed cameras were used with an appropriate combination of prismatic and planar mirrors to split each camera into two views. The Reynolds number was fixed at $Re = 2400$, and the circular jet at the same Reynolds number was also measured for comparison. Fourier mode decomposition was used to identify the large-scale structures superposed in the unsteady flow field. The lobe trough in the jet decreased the jet's width due to the smooth connection between the pipe section and the lobed exit. Turbulence was intensified in the jet shear layer, and the passing fluid puffs in the circular jet instantaneous flow field were also broken in the lobed jet. The successively passing fluid puffs in the circular jet were observed to be the axisymmetric large-scale structure in Fourier modes dominating at $St = 0.39$. However, breakdown of the axisymmetric structures was induced by the lobed nozzle at $St = 0.51$ and 0.65, and the double helical modes arose at $St = 0.28$ and 0.38 (also 0.4) in the shear layer of the jet potential core and interacted with the entire jet column.

Keywords: Dynamics, lobed jet, tomo-PIV, Fourier mode decomposition, helical mode

1. Introduction

Modification of nozzle geometry is extensively applied as a passive control method to either increase jet mixing rate(Gohil et al., 2010; Hu et al., 2001; Mi et al., 2000) or augment the efficiency of jet impingement heat transfer(Koseoglu and Baskaya, 2010; Violato et al., 2012). The lobed nozzle is one of the most attractive nozzle geometries and has been used in numerous experimental and computational investigations(Cooper et al., 2005; Hu et al., 2000). Early studies of free jets that use lobed nozzles revealed a pair of large-scale streamwise vortices at each lobe crest that dominated the jet spreading and mixing processes, whilst the lobe troughs served as mixing tabs in the jet shear layer, which generate counter-rotating streamwise vortex pairs shed from each tab and dramatically increase the mixing layer thickness. A recent study on jet impingement heat transfer using a lobed nozzle comprising three circular orifices revealed that a ratio of the orifice centre offset to the orifice radius of $a/b = 0.8$ (see Figure 1b) yielded the best overall heat transfer enhancement on the target surface(He and Liu, 2018a, 2018b). Accordingly, the large-scale coherent structures in the jet column, i.e., the jet preferred modes(Hussain and Zaman, 1981) must play a fundamental role in the spatiotemporal variation of the jet dynamics using a lobed nozzle.

Lobed nozzles generally feature slender lobes with a periodic distribution that induce alternately directed secondary velocities perpendicular to the mean flow direction. This results in substantial mixing enhancement due to the large-scale streamwise vortices(Belovich and Samimy, 1997; Li et al., 2001). Circular-orifice lobed nozzles are simplified versions that are more convenience to manufacturing in industry(Martin and Buchlin, 2011). The mixing rate in a free lobed jet indeed has a strong association with the slenderness of the lobes: extremely slender lobes induce a significant loss of pressure through the nozzle, which leads to limited application in certain flow configurations. The slenderness of the lobes in a three-orifice lobed nozzle is governed by the ratio of the orifice centre offset to the orifice radius a/b ($a/b = 0$ denotes a circular nozzle). A lower a/b value renders the flow more similar to the case under the control using tabs in the shear layer(Aravindh Kumar and Rathakrishnan, 2017; He and Liu, 2018a, 2018b), thus imposing less modification to the nozzle geometry. It is thus expected to result in a lower pressure loss than with slender-lobed nozzles.

The efficiency of various types of flow control strategies targeted for jet mixing enhancement relies upon the types of flow unsteady mode that can be modified. Various means of control and their effectiveness have been studied to modify the jet shear layer modes without a large pressure loss. Example of these have been the use of indeterminate-origin or crown-shaped nozzles to strengthen the non-uniform thickness of the shear layer on the jet exit plane(Shu et al., 2005a; Shu et al., 2005b; Wlezien and Kibens, 1986)and placement of an axisymmetric ring in the mixing layer near the nozzle exit to modify the shear layer properties and thus the jet spread rate(Parker et al., 2003; Sadeghi and Pollard, 2012). Our recent study(He et al., 2018) proposed the concept of jet preferred mode control with only slight modification of the geometry, but this resulted in a substantial alternation of the flow pattern in the whole jet column and thus a significant mixing enhancement. Unlike the shear layer modes, which originate from shear layer instability, jet preferred modes are large-scale helical and axisymmetric structures that arise from jet global instability and with unstable frequency that scales with the jet diameter(Ball et al., 2012; Hussain and Zaman, 1981). This control mechanism benefits from low pressure drop compared with, for instance, the sweeping jet(Kim and Kim, 2019), and avoids complexity compared with active control methods(Broučková and Trávníček, 2019). Following the concept of our previous study(He et al., 2018), modification of the nozzle exit using lobed geometry would have a substantial effect on the formation of the jet preferred modes(Hussain and Zaman, 1981), which play a significant role in the jet-mixing characteristics and are of particular interest for a fundamental understanding of the flow dynamics.

In this study we concentrate on the dynamical behaviour of the three-dimensional flow in a lobed jet. Measurement are performed using a time-resolved tomographic particle image velocimetry (tomo-PIV) system(Elsinga et al., 2006). Compared to the conventional planar PIV(Ma et al., 2020) and three-dimensional three-component (3D3C) stereo-PIV(Nao et al., 2019) techniques, Tomo-PIV can access the 3D3C velocity fields with relatively high spatial resolution. Two split-screen cameras are configured presently to produce four different views for the particle image capturing. The selection of this a/b value was based on the highest efficiency of impingement heat transfer at a small nozzle-to-plate distance(He and Liu, 2018a, 2018b). Although we did not target jet impingement, the investigation of the flow dynamic features in this lobed jet led to better understanding of the jet mixing

and impingement heat transfer mechanisms. In this study, the Reynolds number was fixed at $Re = 2400$, and a circular jet with the same Reynolds number was also considered for comparison. Fourier mode decomposition was used to identify the large-scale structures superposed in the unsteady flow field.

2. Experimental setup

The experiment was conducted in an octagonal tank (each side, 250 mm; height, 900 mm) filled with tap water, as shown in Figure 1(a). An overflow chamber was designed to control the free surface location and feed the jet flow with the assistance of a frequency-conversion pump. A nozzle with an equivalent diameter $D = 40$ mm was installed at the bottom of the octagonal tank, with the exit 100 mm above the bottom surface to minimise the wall effect on the flow field. Our previous experiments of the impinging jet (He and Liu, 2018a, 2018b) demonstrated that the lobed nozzle with $a/b = 0.8$ yielded the highest heat transfer coefficients on the target surface due to the generation of the energetic vortical structures in the flow with slight modification of the nozzle geometry, we used both a lobed nozzle with $a/b = 0.8$ and a circular nozzle with the same equivalent diameter ($D = 40$ mm; i.e., the same cross-section as the lobed nozzle) for our measurements, as shown in Figure 1(b).

Instead of the orifice configuration previously used in impingement heat transfer(He and Liu, 2018a, 2018b), a new design was used with a circular pipe section connecting the lobed shape (Figure 1(b)) with a smooth transition. This geometry was similar to the transitional lobed nozzle(Belovich and Samimy, 1997) and was expected to exhibit flow features unlike those of the orifice configuration. The jet fluid first entered a stabilising chamber located below the bottom surface of the octagonal tank, which incorporated a cylindrical filter to change the flow direction uniformly from upward to radial and a honeycomb filter with a diameter of $2D$ to damp the large-scale structure and crosswise velocity upstream of the nozzle. The Reynolds number based on the bulk velocity U_0 in the nozzle and the nozzle exit equivalent diameter D used in the experiment was fixed at $Re = 2400$ so as to obtain a clear visualization of the dynamical structures with less turbulence contamination.

The three-dimensional flow-field downstream of the nozzle exit was measured via tomo-PIV. The global seeding of the complete tank was performed with 20-μm hollow glass particles, and illumination was realised by a 25 W continuous-wave laser at 532 nm (Millennia EV25S, USA) with a compacted combination of cylindrical lenses to produce a 25-mm-thick volumetric light on the jet longitudinal plane and a cylinder tank to eliminate the free surface effects on illumination. Two 12-bit

complementary metal-oxide semiconductor (CMOS) cameras (PCO, Germany) with a spatial resolution of 2000 × 2000 pixels and lens (Nikon 50mm/F1.2) with aperture value 11 were used to capture the particle images using a double-exposure mode, i.e., with a sampling rate of 50 image pairs per second, and a time interval of 5 ms between the frames in each image pair yielding a particle shift of approximate 3 pixels in the main region. The particle size was around 3×3 pixels with density of approximately 0.024 Nppp (number of particles per pixel). The exposure time for each image was fixed at 2 ms. Each camera was split into two views, as shown by the yellow dashed line in Figure 1(a), using an appropriate combination of prismatic and planar mirrors(Bardet et al., 2010). This resulted in four different views along the radial direction, each with an image resolution of 1000 × 2000 pixels. This configuration reduced the requirement of the number of cameras but maintained equivalent removal of the ghost particles with the four-camera system. Due to the resolution decreasing of each image caused by the screen splitting, appropriate layout should be designed to keep necessary pixels in the jet region, and attention should be payed to avoid the cross-talking of the particle images from two sides of the split screen. To assess the tomo-PIV results, the planar-PIV measurement was also conducted on the longitudinal plane zooming in to the nozzle exit region.

The camera calibration together with volume self-calibration(Wieneke, 2008) was performed using a dotted-array plane with dot diameter 2.5 mm and distance 20 mm. Three-dimensional calibration was achieved by 25-mm normal shift of the calibration plate controlled by a traverse mechanism within a precision of 0.4%. The velocity vectors were calculated from the raw particle volumes using a TOMOpro code developed in-house(Gan et al., 2012; Worth and Nickels, 2011). In the tomo-PIV measurement, the size of the reconstructed volume was 80 mm (width, x direction) × 200 mm (height, y direction) × 25 mm (thickness, z direction) centred at the nozzle axis. It is important to note that one of the lobe troughs was located on the x axis. Image preprocessing was applied to remove noise and improve the volume reconstructions. The images are first bandpass filtered before background subtraction and local normalization. The multiplicative algebraic reconstruction technique (MART) was used to reconstruct the three-dimensional distribution of the particle grayscale with a resolution of 8 voxels/mm, resulting in a particle sparsity of approximately 2% for the whole reconstructed domain. The sub-voxel accurate PIV algorithm was based on the iterative multigrid volumetric cross-correlation approach with a final pass (minimum) interrogation volume size of 24 ×

24 × 24 voxels and 50% overlap. This yielded a resolution of 26 vectors per nozzle diameter D. A total of 2000 image pairs were captured, resulting in 1000 flow-field snapshots for each jet, spanning approximately 50 oscillation periods of the large-scale structures according to the Strouhal number $St = 0.4$. In the planar-PIV measurement, the camera was zoomed in on the near-nozzle region to measure the velocity profile at the nozzle exit with a higher spatial resolution. Using an interrogation window size of 24 × 24 pixels and a 50% overlap yielded a vector resolution of 50 vectors across the nozzle diameter D. A total of 3000 two-dimensional flow-field snapshots for both jets were obtained for averaging.

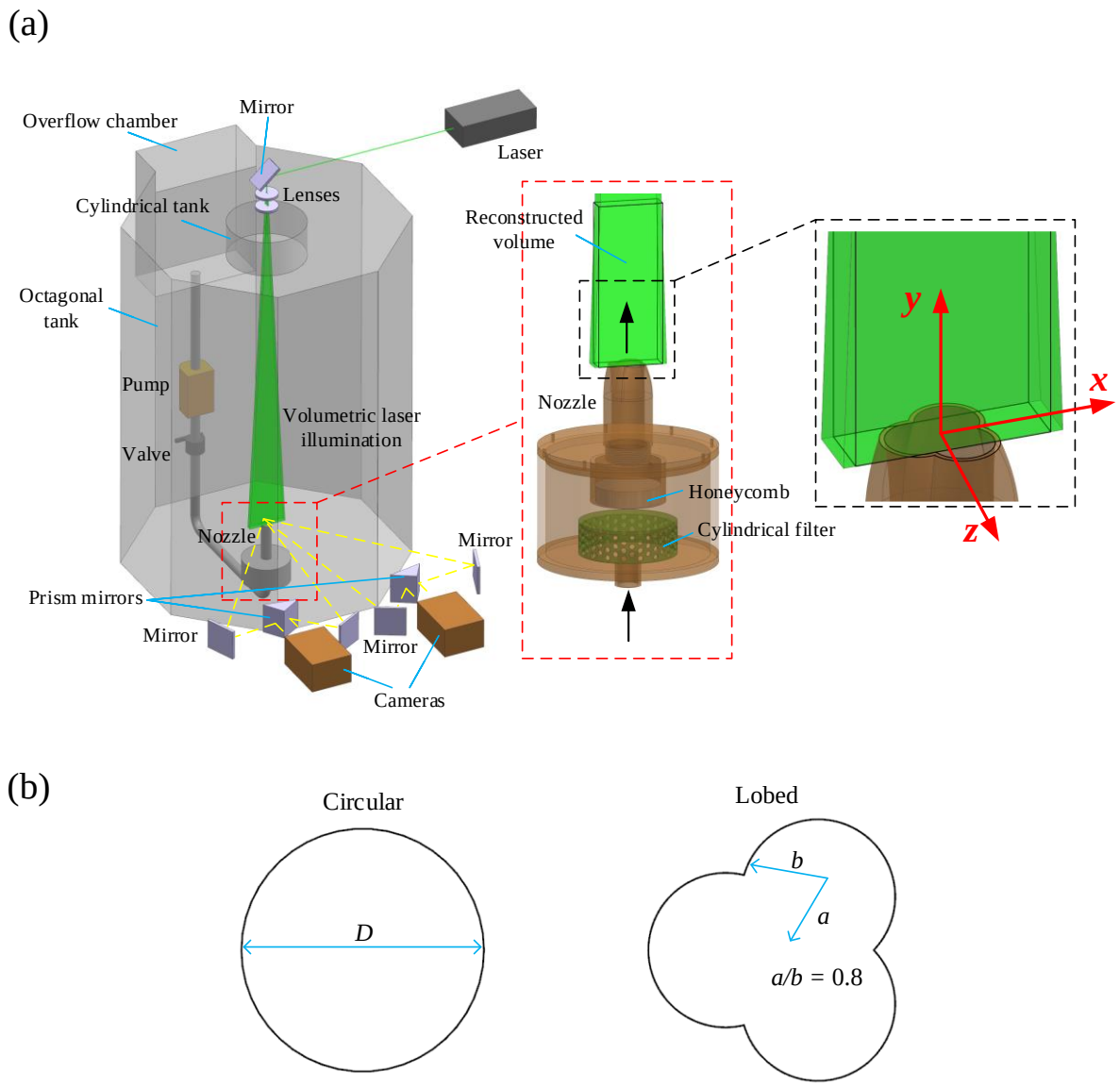

Figure 1. Schematic of (a) experimental setup and (b) nozzle geometry

3. Results and Discussion

3.1 Statistical analysis

Figure 2 shows the time-averaged streamwise velocity profiles and their fluctuations near the nozzle exit at $y/D = 0.125$, which serve to validate the tomo-PIV result with the planar-PIV measurement. It should be noted that the flow field in this region is the most challenging for PIV measurement due to the high shear strain in the jet shear layer. In the planar-PIV measurement, the camera was zoomed onto the near-nozzle region with a higher spatial resolution to effectively capture the top-hat mean velocity profile, with a slight concave shape in the centre, as shown in Figure 2(a) and (b). Due to the lower spatial resolution in the tomo-PIV measurement, the top-hat shape of the mean velocity profile is smoothed out in the shear layer region, whilst the profile matches the planar-PIV measurement reasonably well in other regions. Noticeably, the discrepancy of the planar- and Tomo-PIV measurements in Figure 2(c-d) is induced by the combined effects of the tomography reconstruction error, and ghost particles and size of the interrogational window. The results in Figure 2(c-d) indicate, however, that both the planar-PIV and the tomo-PIV captured significant peaks in the jet shear layer and that these agreed very well with each other.

It is notable that the velocity fluctuation at $|r/D| > 0.5$ measured by the planar-PIV was significantly higher than that of the tomo-PIV, because the laser light intensity in this region was relatively low in the planar-PIV measurement, which induced high levels of noise in vector calculation. It is also notable that the jet width on the lobe trough side ($r/D > 0$) was smaller than that on the lobe crest side ($r/D < 0$), as shown in Figure 2(b); this trend is obviously opposite to the findings in the pure orifice configuration (He and Liu, 2018b) and is discussed in depth in Figure 3. Also see Figure 4 for details regarding the fluctuating velocity increase for the lobed jet shown in Figure 2(c) and (d).

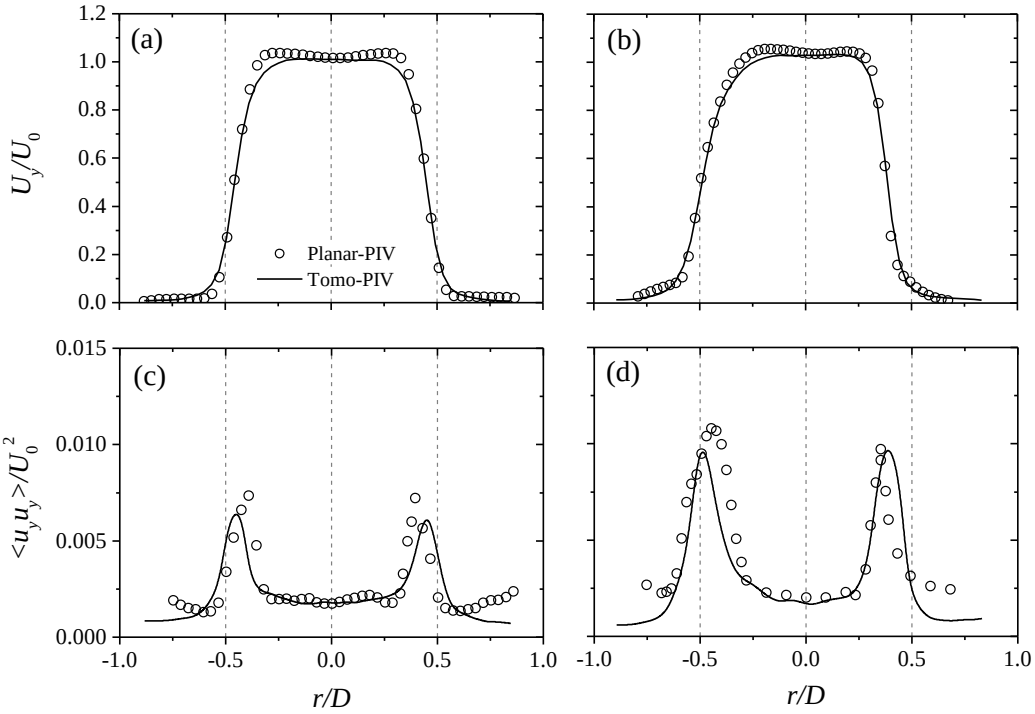

Figure 2. Mean streamwise velocity profiles (a–b) and fluctuation (c–d) at $y/D = 0.125$. (a and c) circular jet and (b and d) lobed jet.

The decrease in the jet width on the lobe trough side did not occur only in the vicinity of the nozzle exit. It occurred even in the far-downstream region as shown in Figure 3, because the jet width remained significantly greater on the crest side ($r/D < 0$) than on the trough side ($r/D > 0$) in the lobed jet, whilst the width on both sides remained roughly equal in the circular jet. When comparing this with the jet-spreading characteristics in the pure orifice configuration (He and Liu, 2018b), one can conjecture that the most likely reason for this asymmetry was the smooth connection between the pipe section and the exit shape in the present lobed nozzle, whilst the 'tap effects' of the lobe trough were weak. This smooth connection caused no flow separation downstream of the lobe trough, which otherwise generated strong vorticity and gave rise to rapid jet spreading in the orifice configuration. The faster decay of the centreline velocity in the lobed jet could also be observed in the contour plot, indicating the higher mixing rate caused by the lobed nozzle.

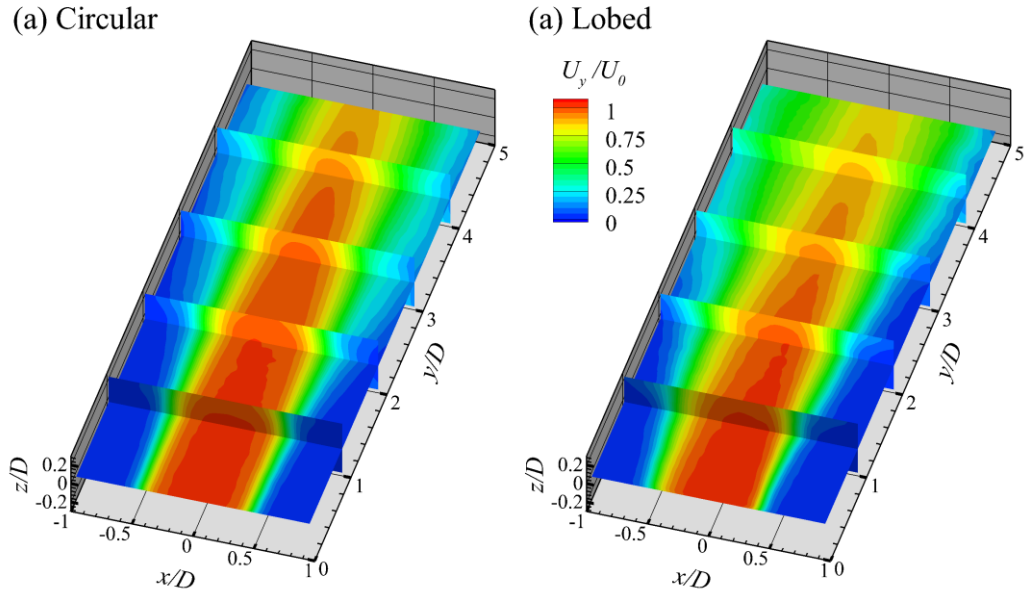

Figure 3. Mean streamwise velocity distributions of (a) circular and (b) lobed jets.

Figure 4 presents the isosurface with turbulent kinetic energy (TKE) $k/U_0^2 = 0.03$ and coloured in terms of the mean streamwise velocity. The contours of the streamwise normal Reynolds stress on the centre plane are also plotted using a greyscale colourmap. In the circular jet, the high TKE concentrated in a narrow jet shear layer, whilst the high-TKE region was enlarged and extended to the nozzle exit in the lobed jet. The upstream extension of the high-KTE region was consistent with the planar-PIV result, as shown in Figure 2(c) and (d), indicating the generation of greater turbulence intensity in the shear layer by the lobed nozzle.

A notable feature of the circular jet is that a region of high TKE was observed in the jet centre at $1.5 < y/D < 3.5$; this was believed to be caused by the large-scale axisymmetric vortex ring, which induced successive puff-like fluid bulks that advected downstream. Figure 5 supports this argument by plotting the instantaneous isosurface of $U_y/U_0 = 0.95$ with the velocity vectors on the centre plane. Thus, successive puff-like fluid bulks can be clearly observed in the circular jet (Figure 5(a)), whilst in the lobed jet, the fluid bulk is broken into small segments downstream of the potential core. Although only one snapshot is shown for each jet, careful inspection of the flow fields for each measured snapshot revealed no large fluid puff (vortex ring-like structure) in the lobed jet advected downstream. One preliminary speculation for this difference is the rapid breakdown of the vortex ring-like structure in the jet potential core, as demonstrated in the literature (Scarano et al., 2010).

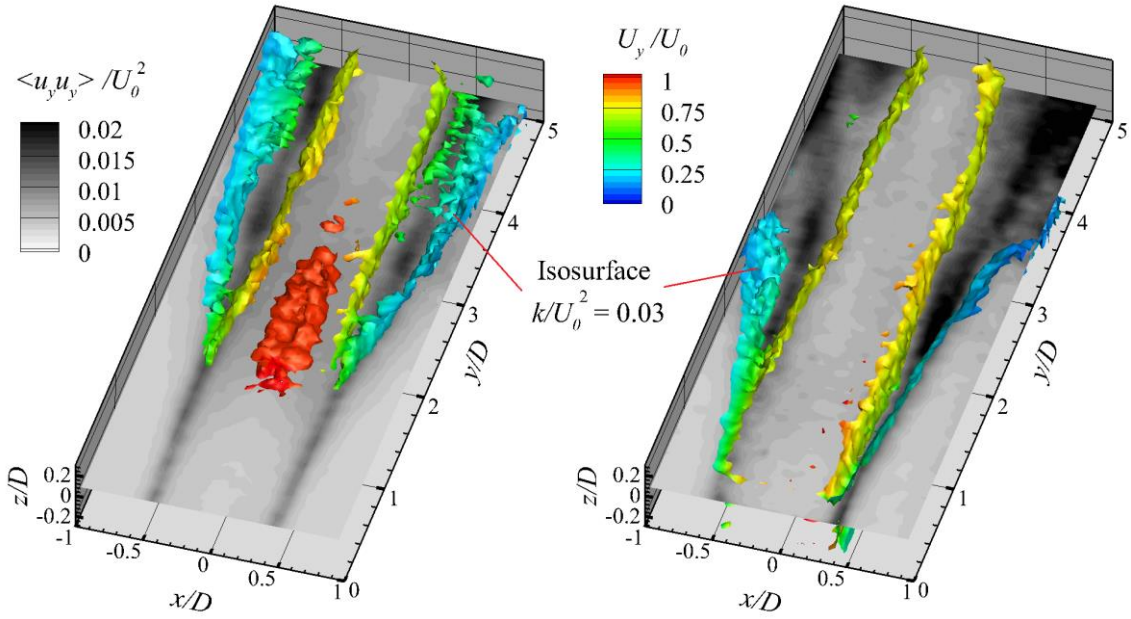

Figure 4. Streamwise normal Reynolds stress (contour) and TKE (isosurface) distributions of (a) circular and (b) lobed jets.

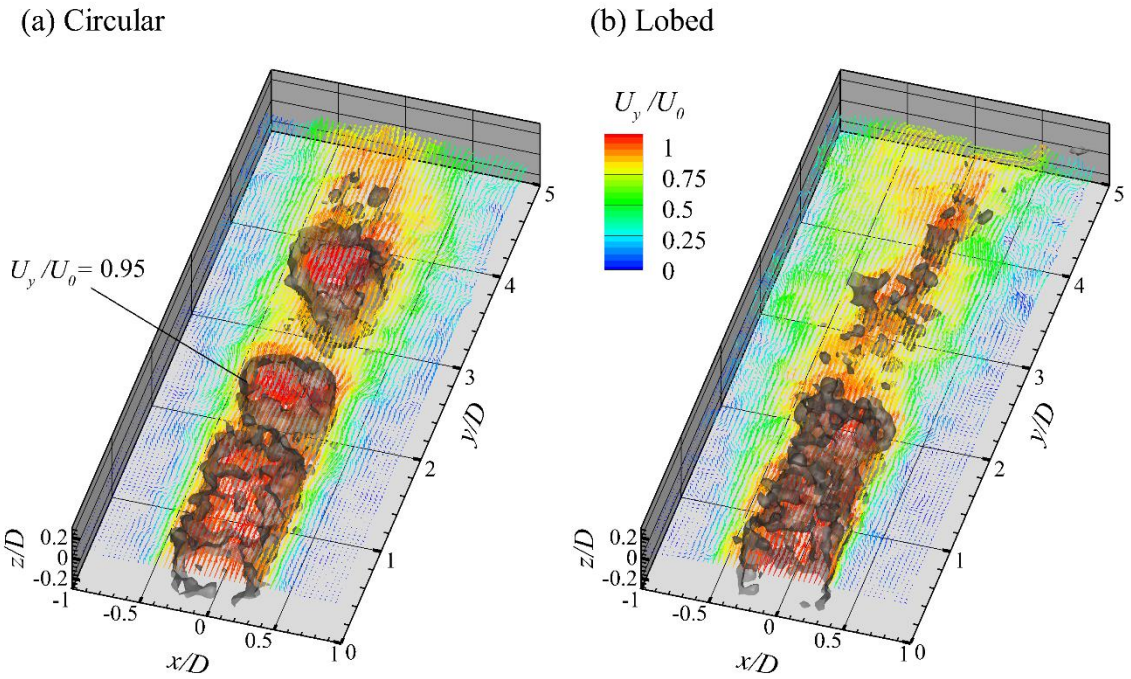

Figure 5. Instantaneous velocity distributions of (a) circular and (b) lobed jets. The isosurface exhibits the streamwise velocity $U_y/U_0 = 0.95$.

3.2 Fourier mode decomposition

This study was performed to determine coherent structures in both circular and lobed jet flows via spectral analysis. First, the power spectral densities (PSDs) at several streamwise locations $y/D = 0.5$, 1.0, 2.0 and 4.0 were inspected. As shown in Figure 6(a) and (b), the PSDs were computed using a window shit technique with 500 time-serial data in each window and 80% overlap; this was shown that the main PSD peaks did not change in frequency when these computational parameters varied. Several spectral peaks coexist in the PSDs of both cases. The lowest spectral peak in both jets is observed at a Strouhal number $St = \frac{fD}{U_0} \approx 0.17$ (f denotes the frequency) at $y/D \geq 2.0$, which is believed to be caused by the experimental apparatus and jet pumping system. This frequency was much lower than that of the coherent structures in jet flows according to a previous study (He and Liu, 2017) and is thus not discussed in detail here.

From $St = 0.27$, one can observe that various peaks coexist with the increasing St and coincide well in frequency for each downstream location in the circular jet, as shown in Figure 6(a). Here, we highlight the most prominent four peaks (i.e., $St = 0.27$, 0.39, 0.51 and 0.65) for further discussion, as higher-frequency peaks denote harmonics or are less coherent and have a much lower PSD. In the lobed jet shown in Figure 6(b), the peaks at $St = 0.51$ and 0.65 are observed at different downstream locations. The lower-frequency peaks at $St = 0.28$ and 0.38, which are close to the peaks in the circular jet, are detected only near the nozzle ($y/D = 0.5$). It is shown below that these peaks are associated with totally different structures than that in the circular jet with similar frequencies. In the region $y/D \geq 1.0$, a peak is observed at $St = 0.33$, which is the median value of 0.28 and 0.38. According to a previous study (Miksad, 1973), this peak at $St = 0.33$ can be considered consequence of the nonlinear interaction of the coherent modes at $St = 0.28$ and 0.38, which occurs only when the amplitude of the basic modes grows large enough and obeys the relationship $St_c = nSt_1/m + pSt_2/q$ ($n = p = 1, m = q = 2$ in this study), where St_c denotes the Strouhal number of the combined mode.

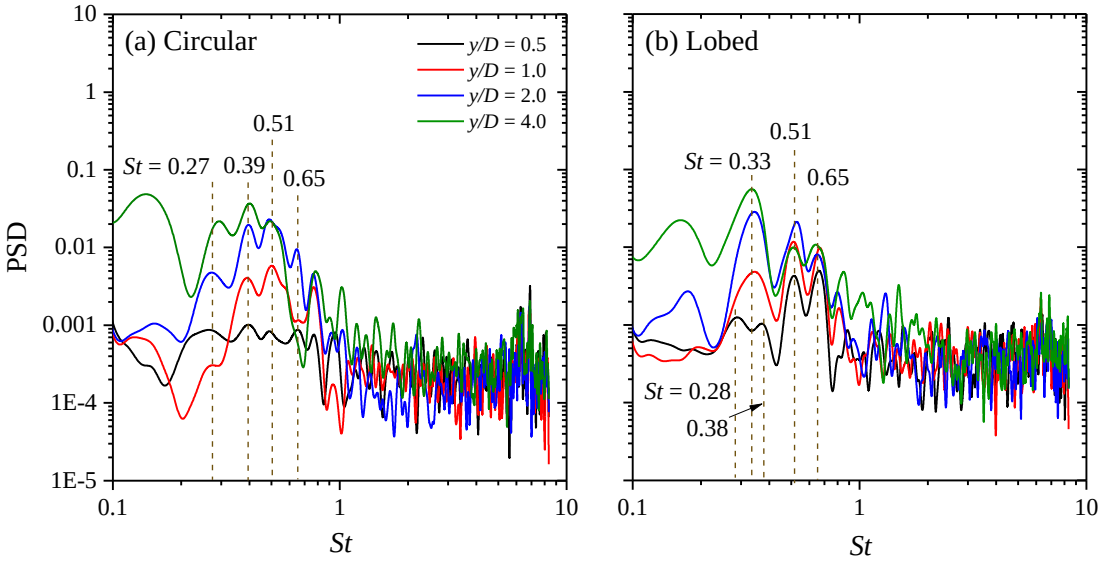

Figure 6. PSDs of streamwise velocity at various downstream locations on jet centreline measured by Tomo-PIV. (a) circular and (b) lobed jets.

Coherent structures at specific frequencies can be identified via mode decomposition techniques such as dynamic mode decomposition(Schmid, 2010) and Fourier mode decomposition(Ma et al., 2015). We selected Fourier mode decomposition as it can be manipulated by means of fast Fourier transform, which is relatively computationally inexpensive. Figure 7 presents the Fourier modes at four PSD peaks in the circular jet. As shown in Figure 7(a), the flow is featured by the shear layer mode at $St = 0.27$. This mode was mainly axisymmetric, and it grew immediately downstream of the nozzle exit and propagated along the jet shear layer. The Fourier mode at $St = 0.39$ denotes the most dominant structure in the jet downstream region, and had a wavelength that coincided with the fluid puff passing in the unsteady field (see Figure 5) and had the largest PSD, as shown in Figure 6(a). In addition, the peaks at $St = 0.51$ and 0.65, presented in Figure 7(c) and (d), respectively, are denoted by higher-order streamwise oscillations inside the jet column. These higher-order streamwise oscillations occurred only within the jet potential core, which broke down into smaller segments further downstream. Each of these modes was mainly axisymmetric according to the three-dimensional shapes of the isosurface; this is also in agreement with the circular jets in previous findings where the Kelvin–Helmholtz instability dominated(Yule, 1978).

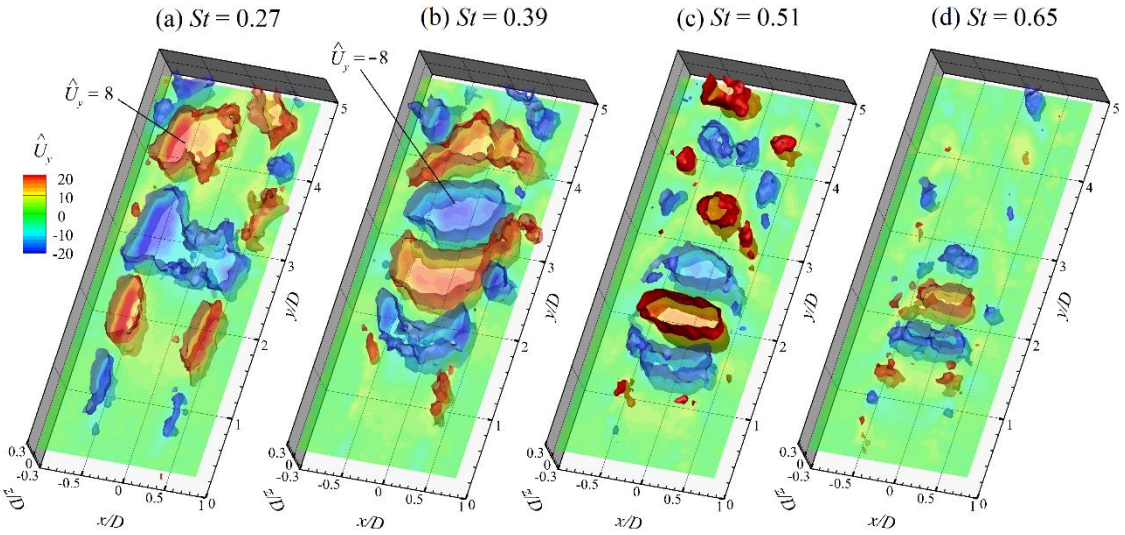

Figure 7. Fourier modes of the flow field in the circular jet. Isosurfaces of streamwise velocity $\widehat{U}_y = 8$ (red) and -8 (blue) are shown together with contours (see legend) on centre plane.

The Fourier modes at the specified St, which are similar or equal to that in the circular jet, are shown in Figure 8. It should be noted that the first two St numbers dominate the PSD only at $y/D = 0.5$, as shown in Figure 6(b). Surveying the mode distribution at $St = 0.28$ and 0.38 shown in Figure 8(a) and (b), different mode shapes can be seen to remain roughly symmetrical with respect to the y-axis, but they are inclined in the azimuthal direction. This feature indicated the existence of helical modes that differ from those shown in Figure 7. Given that these modes prevail throughout the measured streamwise region, but the PSD peaks at $St = 0.28$ and 0.38 do not exist for $y/D > 1.0$, it is reasonable to speculate that strong modes would be generated at various St values that overwhelm the existing modes and thereby become dominant. The modes at $St = 0.51$ and 0.65 present the same physical events as that in the circular jet for the same frequencies, except that each axisymmetric structure has been divided into large organised segments by the lobed nozzle.

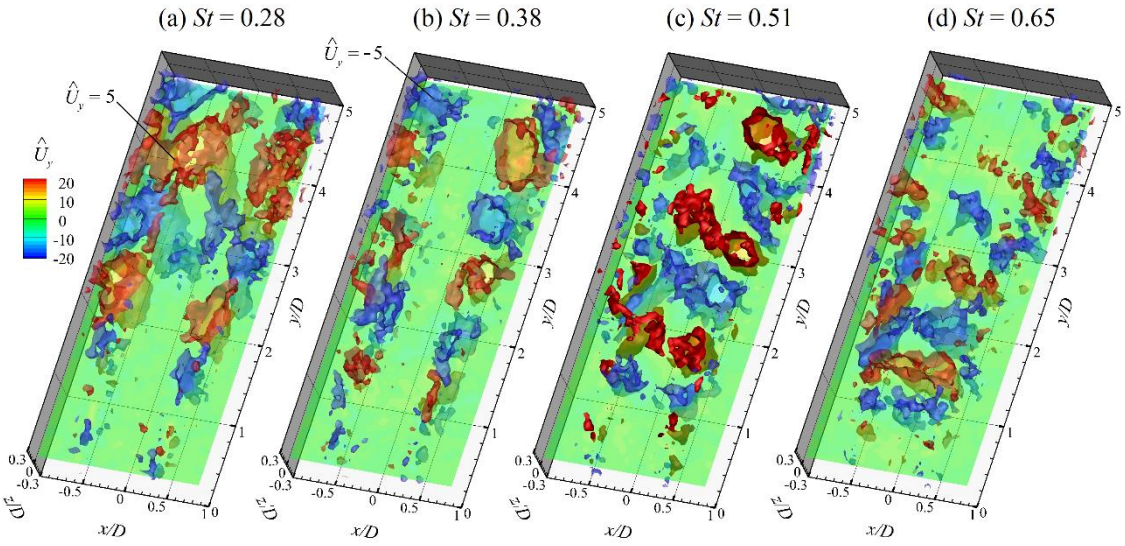

Figure 8. Fourier modes of the flow field in the lobed jet. Isosurfaces of streamwise velocity $\widehat{U}_y = 5$ (red) and -5 (blue) are shown together with contours (see the legend) on centre plane.

To distinguish which helical mode is denoted in Figure 8(a) and (b), Figure 9 presents a detailed description of the Fourier mode at $St = 0.38$ and 0.40. Here, $St = 0.40$ is used as a complement to account for the effects of numerical or experimental error in the frequency determination because the mode sharp at $St = 0.40$ is more obvious. In other words, the modes at $St = 0.38$ and 0.40 ought to be the same event, and the small frequency difference is caused by a numerical or experimental error. In both Figure 8(a) and (b), the inclination of the mode shape exclude the possibility of an axisymmetric mode for this structure, whilst a group of the normal velocity in the z direction on the centre plane (marked by black arrows) provides compelling evidence for a helical structure.

According to the inclines of the mode structure, the direction of the normal velocity component and the rough symmetric sign of the streamwise velocity with respect to the y axis, a double-helical mode (with azimuthal wavenumber $m = 2$ or -2 which will be identified in Figure 11) in the lobed jet can be determined. The double-helical mode is further shown in Figure 10. Here, the isosurface of $\widehat{U}_y = 5$ is shown and coloured by the x coordinate to allow easier viewing of the structures on both sides. The black lines denote the slopes of the mode structures, which indicates the direct connection of these tube-like structures in a three-dimensional domain. According to this, higher-order helical modes such as 4- or 6- helical modes can be excluded, whilst only the double-helical mode remains.

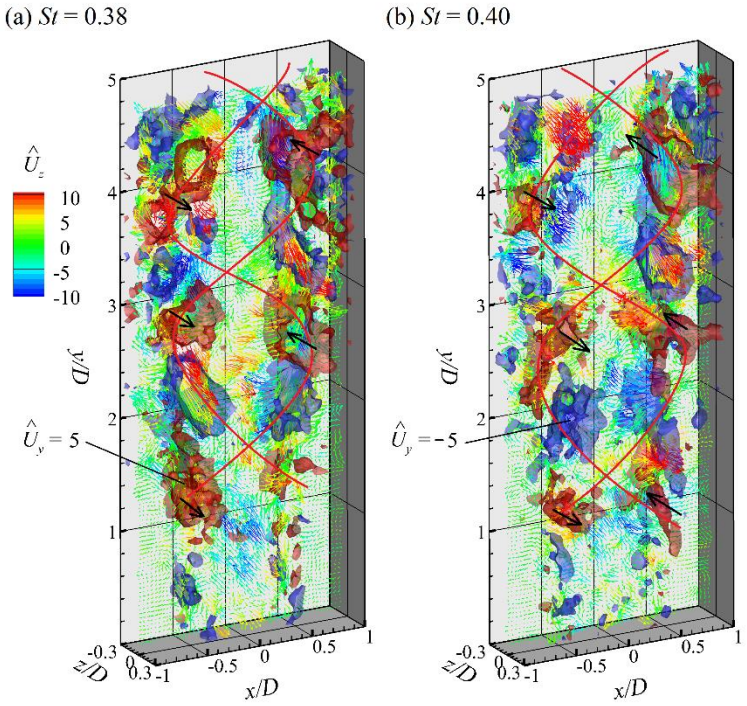

Figure 9. Double helical modes of the flow field in the lobed jet. Isosurfaces of streamwise velocity isosurfaces $\hat{U}_y = 5$ (red) and -5 (blue) are shown together with vectors (coloured by velocity component $\hat{U}_z$, see legend) on centre plane.

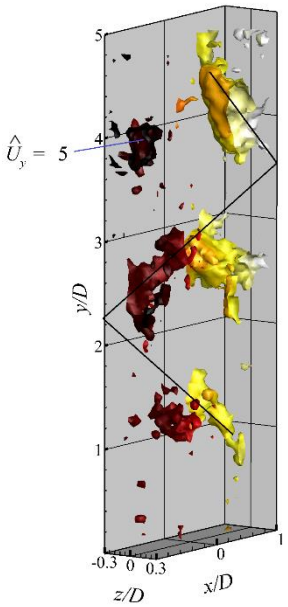

Figure 10. Inclination of the model structure at $St = 0.40$ in the lobed jet. Velocity isosurface $\hat{U}_y = 5$ are shown coloured by x coordinate (darker colour for smaller x).

The temporal variation of the double helical mode is reconstructed by the inverse FFT transformation using the Fourier modes $St = 0.4$. The mean flow field is excluded here to highlight the relatively weak variation of the mode structures. The reconstructed fields at the instances $t = 0, T/4, T/2$ and $3T/4$ are plotted in Figure 11, where T denotes the period corresponding to $St = 0.4$. It is illustrated in the figure that the downstream convection of the mode structure is observed. (Davoust et al., 2012) noted that both the modes $m = 2$ and -2 coexist with opposite helical structures in circular jet, while the anti-clockwise structure ($m = 2$) is more significant in the present lobed one.

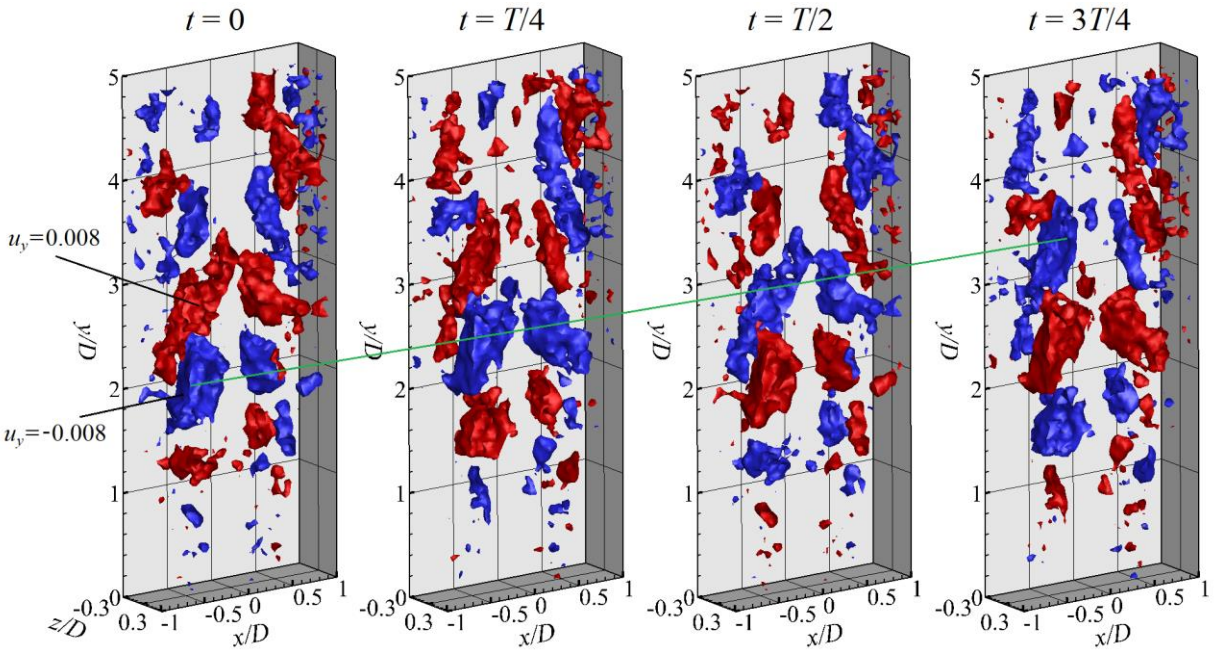

Figure 11.Temporal variation of the double helical Fourier modes in the lobed jet at $St = 0.4$ obtained by inverse FFT transformation. Isosurfaces of the transformed fluctuating velocity $u_y = \pm$ 0.008 are shown. T denotes the period corresponding to $St = 0.4$. The green inclined line indicates the downstream convection of the mode structure.

Figure 12 shows the Fourier mode at $St = 0.33$ in the lobed jet. According to the frequency value, the most likely reason for the generation of this mode was the nonlinear interaction of the modes at $St = 0.28$ and 0.38. The complex sharp of the mode makes it difficult to distinguish the axisymmetric and helical modes. Nevertheless, some clues to this mode can be found in the instantaneous flow field, as shown in Figure 5(b), where the isosurface of the jet column suddenly ends at $y/D \approx 2.4$ and then breaks down, with the bulk of segments advected downstream. This phenomenon roughly agrees with the mode shape shown in Figure 12, where a large velocity amplitude arises in the region of $y/D = 2.0$

– 3.0.

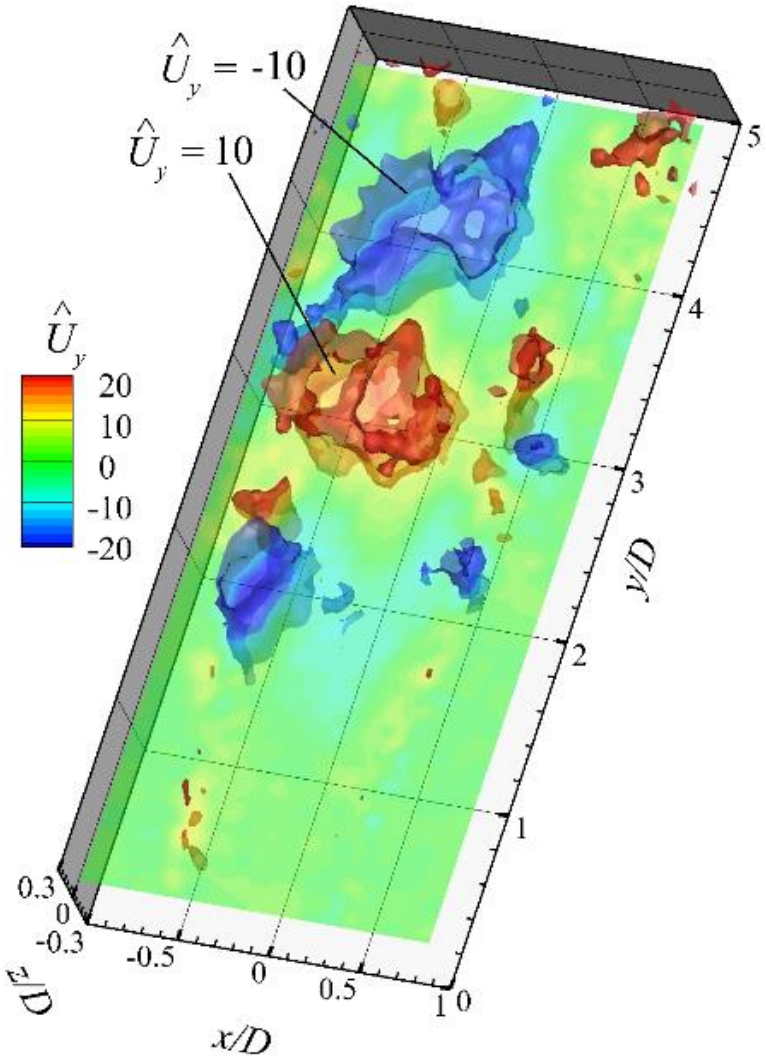

Figure 12. Fourier modes of the flow field in the lobed jet at $St = 0.33$. Isosurfaces of streamwise velocity $|\hat{U}_y| = 10$ are shown together with contours on centre plane.

It is clear that the flow dynamic features in the circular and lobed jets differed greatly. In the circular jet, the axisymmetric large-scale structure dominated the flow field, with bulks of vortex ring-like structures passing successively. Although similar but fragmented ring structures also existed in the lobed jet, this was not a direct result of breakdown of axisymmetric structures. The breakdown of the axisymmetric structures induced by the lobed nozzle occurred at $St = 0.51$ and 0.65, whilst the double helical modes that arose at $St = 0.28$ and 0.38 and existed in the shear layer of the jet potential core interact, which affected the whole jet column. It was also interesting to note that no triple-helical mode

was observed in the lobed jet, even though a three-orifice nozzle was used in the measurement. This may be associated with the more rapid decay of the higher-order modes, whilst the axisymmetric, single-helical or double-helical modes dominate the flow potential core and the downstream field(Jung et al., 2004; Tso and Hussain, 1989).

4. Concluding Remarks

This study used tomo-PIV measurement to examine the large-scale coherent structures that prevailed in a smooth-transition lobed jet. The equivalent diameter of the nozzle exit was $D = 40$ mm, and the thickness of the reconstructed domain was 25 mm. A circular jet with the same diameter was also measured as a reference for comparison. The Reynolds number was fixed at $Re = 2400$.

Unlike the orifice configuration, the lobe trough in the jet in this study did not work as the mixing tab to increase the jet-spreading rate; in contrast, the jet width was decreased due to the smooth connection between the pipe section and the lobed exit. Nevertheless, the lobed nozzle intensified the turbulence in the jet shear layer and broke the passing fluid puff that existed in the circular jet instantaneous flow field.

The successively passing fluid puff in the circular jet was observed to be the axisymmetric large-scale structure in Fourier modes dominating at $St = 0.39$. An axisymmetric mode was observed at other St numbers in the circular jet, but the breakdown of the axisymmetric structures induced by the lobed nozzle occurred at $St = 0.51$ and 0.65, which had little effect on the jet's large-scale unsteady feature. Meanwhile, double-helical modes arose at $St = 0.28$ and 0.38 (also 0.4), which existed in the shear layer of the jet potential core and interacted, affecting the whole jet column.

Acknowledgements

The authors gratefully acknowledge financial support for this study from the National Natural Science Foundation of China (11725209, 12002208), the Engineering and Physical Sciences Research Council of the UK (EP/P004377/1) and Key Laboratory of Aerodynamic Noise Control (ANCL20190302)

References

Aravindh Kumar, S., Rathakrishnan, E., 2017. Elliptic jet control with triangular tab. Proceedings of the Institution of Mechanical Engineers, Part G: Journal of Aerospace Engineering 231, 1460-1477.

Ball, C.G., Fellouah, H., Pollard, A., 2012. The flow field in turbulent round free jets. Progress in Aerospace Sciences 50, 1--27.

Bardet, P.M., Peterson, P.F., Savaş, Ö., 2010. Split-screen single-camera stereoscopic PIV application to a turbulent confined swirling layer with free surface. Experiments in Fluids 49, 513-524.

Belovich, V.M., Samimy, M., 1997. Mixing processes in a coaxial geometry with a central lobed mixer-nozzle. AIAA journal 35, 838-841.

Broučková, Z., Trávníček, Z., 2019. Intermittent round jet controlled by lateral pulse-modulated synthetic jets. Journal of Visualization 22, 459–476.

Cooper, N., Merati, P., Hu, H., 2005. Numerical simulation of the vortical structures in a lobed jet mixing flow, 43rd AIAA Aerospace Sciences Meeting and Exhibit, Reno, Nevada, p. 635.

Davoust, S., Jacquin, L., Leclaire, B., 2012. Dynamics of m = 0 and m = 1 modes and of streamwise vortices in a turbulent axisymmetric mixing layer. Journal of Fluid Mechanics 709, 408-444.

Elsinga, G.E., Scarano, F., Wieneke, B., Oudheusden, B.W.V., 2006. Tomographic particle image velocimetry. Experiments in Fluids 41, 933-947.

Gan, L., Cardesa-Duenas, J., Michaelis, D., Dawson, J., 2012. Comparison of Tomographic PIV algorithms on resolving coherent structures in locally isotropic turbulence, 16th International Symposium on Applications of Laser Techniques to Fluid Mechanics, , Lisbon, Portugal.

Gohil, T.B., Saha, A.K., Muralidhar, K., 2010. Control of flow in forced jets: A comparison of round and square cross sections. Journal of Visualization 13, 141-149.

He, C., Liu, Y., 2017. Proper orthogonal decomposition of time-resolved LIF visualization: scalar mixing in a round jet. Journal of Visualization 20, 789-815.

He, C., Liu, Y., 2018a. Jet impingement heat transfer of a lobed nozzle: Measurements using temperature-sensitive paint and particle image velocimetry. International Journal of Heat and Fluid Flow 71, 111-126.

He, C., Liu, Y., 2018b. Large-eddy simulation of jet impingement heat transfer using a lobed nozzle. International Journal of Heat and Mass Transfer 125, 828-844.

He, C., Liu, Y., Yavuzkurt, S., 2018. Large-eddy simulation of circular jet mixing: lip-and inner-ribbed nozzles. Computers & Fluids 168, 245-264.

Hu, H., Kobayashi, T., Saga, T., Segawa, S., Taniguchi, N., 2000. Particle image velocimetry and planar laser-induced fluorescence measurements on lobed jet mixing flows. Experiments in Fluids 29, S141-S157.

Hu, H., Saga, T., Kobayashi, T., Taniguchi, N., 2001. A study on a lobed jet mixing flow by using stereoscopic particle image velocimetry technique. Physics of Fluids 13, 3425-3441.

Hussain, A.K., Zaman, K.B., 1981. The ‘preferred mode’ of the axisymmetric jet. Journal of Fluid Mechanics 110, 39-71.

Jung, D., Gamard, S., George, W.K., 2004. Downstream evolution of the most energetic modes in a turbulent axisymmetric jet at high Reynolds number. Part 1. The near-field region. Journal of Fluid Mechanics 514, 173-204.

Kim, S., Kim, H., 2019. Quantitative visualization of the three-dimensional flow structures of a sweeping jet. Journal of Visualization 22, 437-447.

Koseoglu, M., Baskaya, S., 2010. The role of jet inlet geometry in impinging jet heat transfer, modeling and experiments. International Journal of Thermal Sciences 49, 1417-1426.

Li, H., Hu, H., Kobayashi, T., Saga, T., Taniguchi, N., 2001. Visualization of multi-scale turbulent structure in lobed mixing

jet using wavelets. Journal of Visualization 4, 231-238.
Ma, L., Feng, L., Pan, C., Gao, Q., Wang, J., 2015. Fourier mode decomposition of PIV data. Science China Technological Sciences 58, 1935-1948.
Ma, X., Tang, Z., Jiang, N., 2020. Visualization of Lagrangian fluid transport of a vortex ring based on time-resolved PIV. Journal of Visualization 23, 559–564.
Martin, R.H., Buchlin, J., 2011. Jet impingement heat transfer from lobed nozzles. International Journal of Thermal Sciences 50, 1199-1206.
Mi, J., Nathan, G., Luxton, R., 2000. Centreline mixing characteristics of jets from nine differently shaped nozzles. Experiments in Fluids 28, 93-94.
Miksad, R.W., 1973. Experiments on nonlinear interactions in the transition of a free shear layer. Journal of Fluid Mechanics 59, 1-21.
Nao, Ninomiya, Yukihisa, Tanaka, Satoshi, Sotome, Masahide, Eda, Atsushi, Watanabe, 2019. 3-D measurement of 2-D jet by 3-D 3-C SPIV. Journal of Visualization 22, 305 – 312.
Parker, R., Rajagopalan, S., Antonia, R.A., 2003. Control of an axisymmetric jet using a passive ring. Experimental Thermal and Fluid Science 27, 545-552
Sadeghi, H., Pollard, A., 2012. Effects of passive control rings positioned in the shear layer and potential core of a turbulent round jet. Physics of Fluids 24, 3943-3973.
Scarano, F., Bryon, K., Violato, D., 2010. Time-resolved analysis of circular and chevron jets transition by tomo-PIV, 15th International Symposium on Applications of Laser Techniques to Fluid Mechanics Lisbon, Portugal.
Schmid, P.J., 2010. Dynamic mode decomposition of numerical and experimental data. Journal of Fluid Mechanics 656, 5-28.
Shu, F., Plesniak, M., Sojka, P., 2005a. Visualization of streamwise vortex pairs in an indeterminate origin (IO) nozzle jet. Journal of Visualization 8, 195-195.
Shu, F., Plesniak, M.W., Sojka, P.E., 2005b. Indeterminate-origin nozzles to control jet structure and evolution. Journal of Turbulence, N26.
Tso, J., Hussain, F., 1989. Organized motions in a fully developed turbulent axisymmetric jet. Journal of Fluid Mechanics 203, 425-448.
Violato, D., Ianiro, A., Cardone, G., Scarano, F., 2012. Three-dimensional vortex dynamics and convective heat transfer in circular and chevron impinging jets. International Journal of Heat and Fluid Flow 37, 22-36.
Wieneke, B., 2008. Volume self-calibration for 3D particle image velocimetry. Experiments in Fluids 45, 549-556.
Wlezien, R.W., Kibens, V., 1986. Passive control of jets with indeterminate origins. AIAA journal 24, 1263-1270.
Worth, N., Nickels, T., 2011. Time-resolved volumetric measurement of fine-scale coherent structures in turbulence. Physical Review E 84, 025301.
Yule, A., 1978. Large-scale structure in the mixing layer of a round jet. Journal of Fluid Mechanics 89, 413-432.